ADVANCED ENERGY MATERIALS
www.advenergymat.de

Insights on SEI Growth and Properties in Na-Ion Batteries via Physically Driven Kinetic Monte Carlo Model

*Kie Hankins, Miftahussurur Hamidi Putra, Janika Wagner-Henke, Axel Groß, and Ulrike Krewer**

Sodium-ion batteries (SIBs) show promise for the next generation of energy storage technology but face significant challenges in regards to stability due in part to uncontrolled degradation of the solid electrolyte interphase (SEI). Kinetic Monte Carlo (kMC) modeling is uniquely suited to provide molecular-scale insight on the phenomena that influence SEI growth and behavior in SIBs over full charge. In this work, spatially- and time-dependent electrical potential is incorporated into kMC modeling for the first time, which enables the precise study of electrochemical reactivity and SEI growth during charging. A reaction network for a carbonate/$NaPF_6$ electrolyte developed using density functional theory is used to power the kMC simulations. The decomposition of $NaPF_6$ and formation of NaF is unfavorable at standard conditions, suggesting that water or other contaminants are required to facilitate the reaction. The SEI is shown to be primarily made of Na_2CO_3. SEIs with low electric conductivities exhibit the most ideal behavior and high C-rates generate thinner SEIs with greater fractions of organic species. Dissolution of SEI species is shown to occur rapidly, even during formation. The results of the model correspond well to the SEI behavior known in the literature, and reveal the fundamental mechanisms that influence cell behavior.

1. Introduction

The availability of large-scale, efficient, and dynamic energy storage technologies is one of the primary roadblocks in the transition away from fossil-fuel based energy sources. Lithium-ion batteries (LIBs) are one of the most popular energy storage technologies today due to their high energy density and stability. However, due to their chemical components, LIBs have several significant deficiencies that inhibit their widespread use in grid-scale energy storage and electric vehicles.[1–3] They contain several elements, such as lithium, cobalt, and copper, that are relatively rare and unevenly distributed throughout the globe. This leads to geopolitical challenges and high production costs.[4] Several of their components are also toxic and environmentally damaging.

Sodium-ion batteries (SIBs) have emerged as promising candidates for the next generation of energy storage systems, offering the potential to address many of the limitations associated with their lithium-ion counterparts. The gravimetric energy density of SIBs is notably lower than that of LIBs. However, this discrepancy holds relatively minor importance in the context of stationary energy storage, where weight considerations are significantly diminished.[5] The attractiveness of SIBs is primarily rooted in the abundance of sodium throughout the globe, which reduces concerns regarding resource availability, geopolitical dependencies, and environmental sustainability. This abundance also allows for substantially lower production costs, which would enable widespread implementation of grid-scale energy storage. There has been significant progress in SIB research in recent years, and they have recently been produced commercially for the first time.[6–9] However, the continued growth of sodium-ion technology on a commercial scale is contingent upon overcoming a number of critical challenges.

One of the most crucial aspects of SIBs is the formation and management of the solid electrolyte interphase (SEI), a film consisting of decomposed electrolyte species that forms on the surface of the negative electrode. The SEI serves to protect the electrode surface by inhibiting continued reductive decomposition of the electrolyte while facilitating Na^+ transport, and plays an integral role in the overall performance, safety, and cycle life of the battery.[10] The SEIs in SIBs are more complex and less stable than their LIB counterparts; this instability leads to uncontrolled consumption of the electrolyte and eventual cycling failure of the battery.[11–13] Considerable recent research efforts have been di-

K. Hankins, J. Wagner-Henke, U. Krewer
Institute for Applied Materials - Electrochemical Technologies
Karlsruhe Institute of Technology
Adenauerring 20b, 76131 Karlsruhe, Germany
E-mail: Ulrike.Krewer@kit.edu
M. H. Putra, A. Groß
Institute for Theoretical Chemistry
Ulm University
Oberberghof 7, 89081 Ulm, Germany
The ORCID identification number(s) for the author(s) of this article can be found under https://doi.org/10.1002/aenm.202401153

DOI: 10.1002/aenm.202401153

rected toward understanding the properties and failure modes of the SEI in SIBs.[14,15]

Prior knowledge from LIBs can be used as a baseline and point of comparison for the study of the SEI in SIBs. The SEIs in SIBs exhibit significantly different properties and behaviors compared to their LIB counterparts. $NaPF_6$ has been shown to be more stable than $LiPF_6$,[16] which leads to a significantly reduced amount of fluoride species and increased amount of carbonates in the SEI. The SEI is known to be composed primarily of Na_2CO_3, NaF, and organic carbonates, but the ratios and specific details of the organic species are uncertain.[14,17–19] Overall, the growth processes, chemistry, and structure of the SEI, especially at the nanometric scale, are not well-understood.

The dissolution of SEI components has been proposed as a major mechanism of SEI failure.[20] This is due to the relatively high solubility of Na-based SEI species compared to their lithium analogs.[11] Research has been dedicated to engineering SEIs with less soluble components, and searching for solvent species that have a lower solubility of the SEI components.[21] Experimental studies have noted enhanced performance in cells utilizing electrolyte mixtures containing ethylene carbonate (EC) and propylene carbonate (PC) when compared to cells with pure PC. This improved performance is likely due to increased SEI stability, but the exact mechanistic reason is unclear.[22,23] The underlying mechanism may be chemical in nature, where PC contributes to the formation of SEIs with different chemical compositions, or physico-chemical, where PC alters ion transport mechanisms/kinetics or the solubility of SEI components.[24–26] Understanding the underlying mechanisms of the improved performance of EC/PC solvents is vital to guide the development of effective SIB electrolytes.

The C-rate of the cell during first formation is widely known to have a significant impact on SEI properties and cell performance. Slower C-rates have historically been used with LIBs during first formation, and have been shown to improve SEI stability, capacity retention, and cell cycle life.[27,28] More recently, studies have shown that medium and high C-rates can reduce consumption of active material and irreversible capacity loss in the first cycle,[29] and generate thinner and more uniform SEIs in SIBs.[30] These studies indicate that the C-rate has a complex effect on SEI formation, and there is a trade-off between consumption of active material during the first cycle and long-term capacity retention, but the molecular processes that drive these behaviors are not well understood.

The determination of the underlying mechanism of SEI formation, and understanding SEI behavior in general, is challenging because it is driven by molecular-scale properties and processes that unfold over the scales of seconds and hours.[31] Classical molecular dynamics simulations are able to capture detailed atomistic phenomena at the interface, but are limited to relatively short timescales and thus cannot capture the behavior and degradation of the SEI during charging.[32] On the other side, continuum models are able to simulate electrode and interfacial behavior at long timescales,[33,34] but are not able to resolve the detailed nanoscale phenomena that drive SEI properties. Kinetic Monte Carlo (kMC) modeling is ideal for the study of SEI growth and behavior because it is able to provide molecular-scale insights over practical time and length scales.[35–37] Coupling such a kMC model with a continuum cell model containing a charge balance, allows to model SEI formation over a complete charge process, including spatial and temporal changes in potential, SEI composition, SEI thickness, and impact of C-rate or particle size.[38,39]

In this work, we introduce the first kMC model featuring dynamic and spatially-dependent electric potentials, enabling a more physically-motivated representation of charging behavior. This model facilitates a comprehensive understanding of the fundamental molecular mechanisms that drive SEI growth and behavior throughout full charge cycles. The incorporation of dynamic and spatial elements in the potential enhances the model's capability to capture intricate electrochemical details and offers valuable insights into the nuanced behavior of the SEI under various charging conditions. The specific decomposition pathways and mechanisms considered in this study were derived for density functional theory (DFT) calculations that are well suited to elucidate atomistic processes in batteries.[40] Herein, we study SEI growth in SIBs with kMC modeling for the first time, with a specific focus on elucidating the influences of electrolyte chemistry, electrochemical conditions, and diffusive and dissolution properties on the growth of the SEI on the hard carbon anode of an EC/PC/$NaPF_6$ SIB system without impurities or additives. This serves as a solid basic system that can be extended with impurities, additives and special surface properties of hard carbon.

2. Results and Discussion

KMC calculations were performed for 11 different system conditions in order to study the influence of chemistry, electrochemical properties, and dissolution or diffusion on SEI growth and characteristics. Specifically, solvent composition, i.e., the ratio of EC to PC, electrical conductivity, molecular diffusivity, and C-rates, were varied. The specific conditions of each system are listed in **Table 1**. For clarity, NaF, Na_2CO_3, and PF_x are defined as inorganic species, and all other SEI components are defined as organic species. In the following, we will first characterize the properties of our baseline system which consists of a 1:1 EC:PC (wt) electrolyte with 1 M $NaPF_6$ over a hard carbon electrode. The effects of electrolyte composition will then be studied by considering 1:9 and 9:1 EC:PC mass ratios. Furthermore, the influence of the electrochemical conditions on SEI formation will be addressed by modifying the electronic conductivities and the charging rates. Finally, the effects of diffusion and dissolution will be assessed.

2.1. SEI Growth and Insight—First Insights

System A is used as the baseline configuration for comparison with other systems; it contains a 1:1 EC:PC electrolyte with 1 M $NaPF_6$ in contact with a hard carbon electrode, which is charged at 0.25 C. The time evolution of the SEI during charging is shown in **Figure 1**. Significant dissolution of the SEI, marked by the visibly lower density of SEI species, is observable at the top of the SEI, which corresponds well to experimentally observed behavior.[11] The different species are homogeneously distributed throughout the SEI and there is no visible or quantifiable evidence of layering or clustering. Clustering and layering have been previously observed in our kMC simulations for SEI growth on Li metal,[36,41]

Table 1. Overview of studied system conditions for kMC simulations of SEI growth during the first charge of a Na / Hard carbon intercalation anode; varied parameters include the solvent composition, SEI electronic conductivity κ_S, C-rate, diffusion rate, and initial state.

System	EC:PC [wt]	κ_S S m^{-1}	C-rate	Notes
A	1:1	$1.05 \cdot 10^{-10}$	0.25	Baseline
B	1:9	$1.05 \cdot 10^{-10}$	0.25	
C	9:1	$1.05 \cdot 10^{-10}$	0.25	
D	1:1	$5 \cdot 10^{-11}$	0.25	
E	1:1	$2.00 \cdot 10^{-10}$	0.25	
F	1:1	$1.05 \cdot 10^{-10}$	0.1	
G	1:1	$1.05 \cdot 10^{-10}$	1	
H	1:1	$1.05 \cdot 10^{-10}$	0.25	2x global diffusion rate prefactor
I	1:1	$1.05 \cdot 10^{-10}$	0.25	5x global diffusion rate prefactor
J	1:1	$1.05 \cdot 10^{-10}$	0.25	2x global diffusion rate prefactor, increased organic and decreased inorganic diffusion[a)]
K	1:1	$1.05 \cdot 10^{-10}$	0.25	2 nm native Na_2CO_3 SEI

[a)] Modified binding energies were used to manipulate inorganic and organic diffusion in system J, specific values are listed in the methodology section.

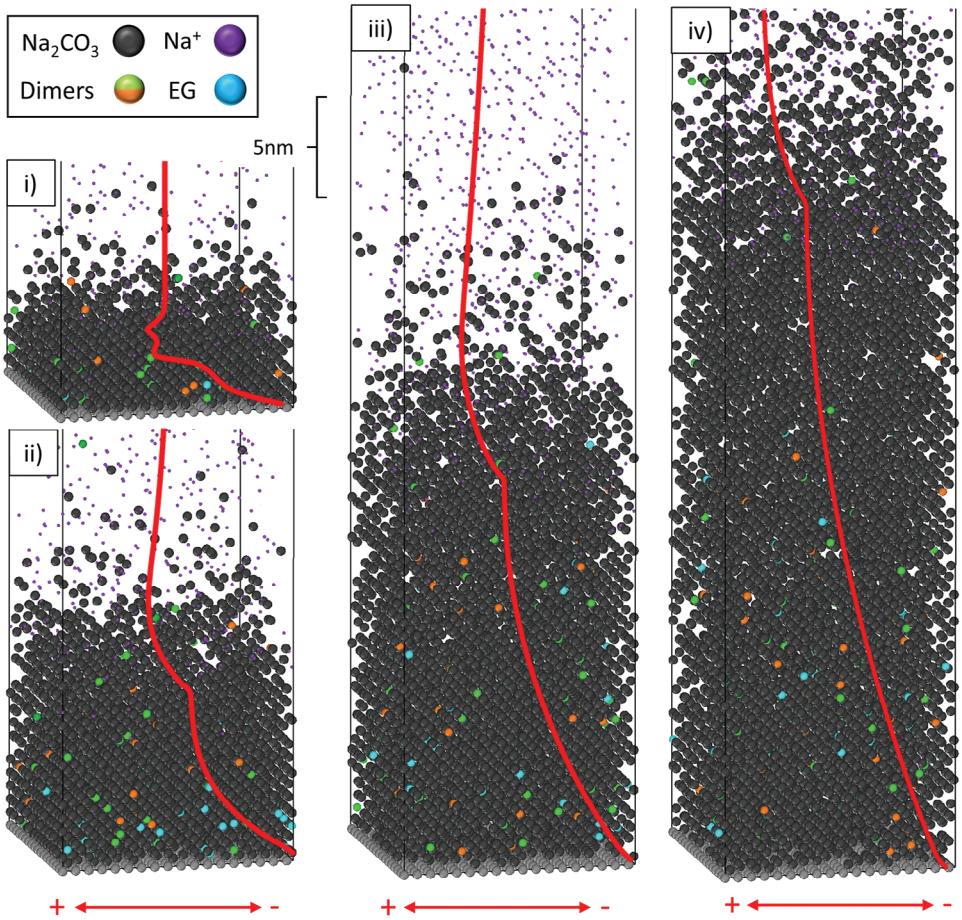

Figure 1. Evolution of the SEI and corresponding potential curves throughout first charge at 0.25 C of a hard carbon electrode in 1:1 EC:PC 1 M $NaPF_6$ electrolyte (system A). simulation, with potential decreasing from left to right at i) SOC = 0.07%, ii) SOC = 6%, iii) SOC = 30%, and iv) SOC = 100%. The green and orange "Dimers" correspond to $NaCO_3CH_2CH_2CO_3Na$ and $NaCO_3CH_2C(CH_3)HCO_3Na$, the blue "EG" species correspond to ethylene glycol ($NaOCH_2CH_2ONa$, and the hard carbon electrode is depicted as a grey surface.

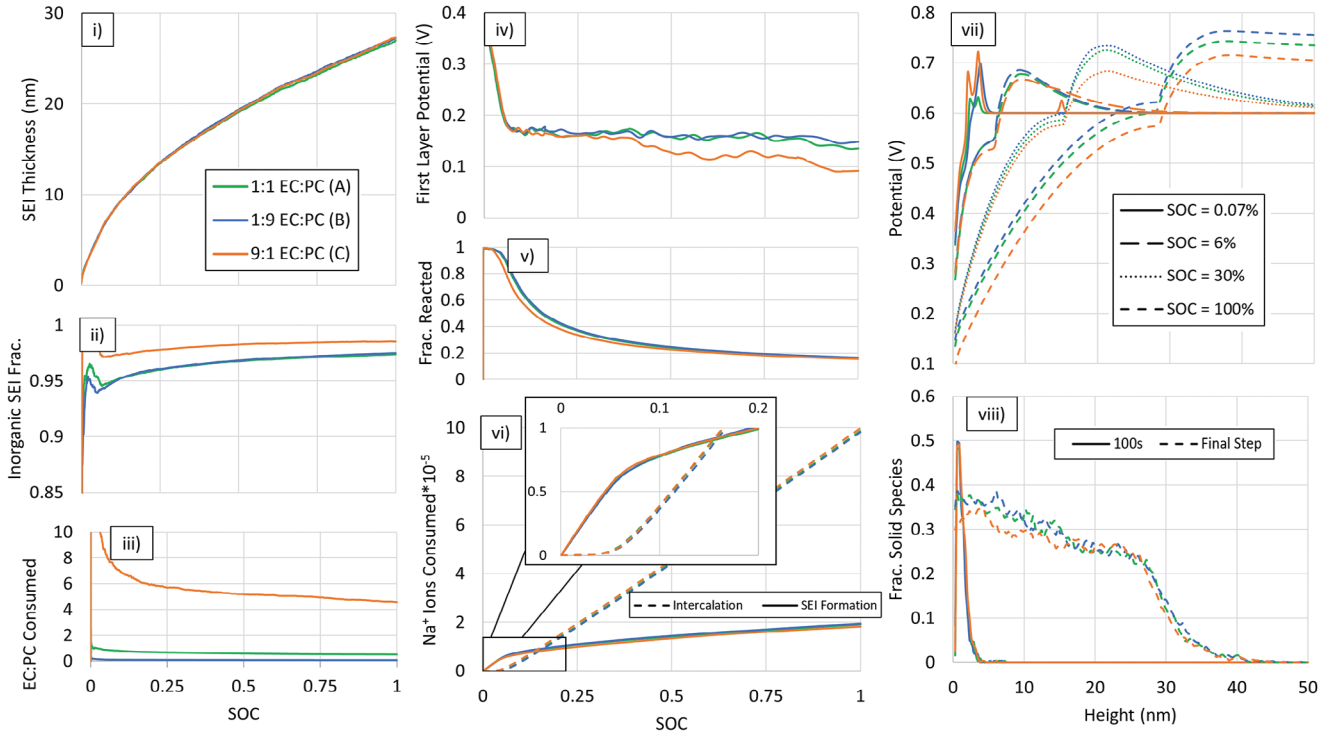

Figure 2. Impact of solvent composition, i.e., EC:PC = 1:1 A), 1:9 B) or 9:1 C) on SEI evolution and properties during a full charge. i) SEI thickness, ii) The molar fraction of the SEI that is inorganic, iii) Molar ratio of EC to PC consumed, iv) Electric potential of the first SEI layer at the electrode surface, v) Molar Fraction of Na^+ consumed for SEI formation versus intercalation, vi) Amount of intercalation and SEI formation reactions, vii) Spatial potential at different SOC, viii) Fraction of sites occupied by solids at a given height at SOC =1.

the absence of these structures here is likely due to the assumed high diffusivity of the Na-based species. More details on this diffusivity are provided in the methodology.

Calculations revealed that the standard $NaPF_6$ decomposition path[42] has a high reduction potential and unfavorable reactivity at system conditions. No $NaPF_6$ decomposition (Equation 10) occurred during any of the kMC simulations in this work. This indicates that the $NaPF_6$ decomposition and NaF formation observed experimentally are induced by another source, such as water contamination.[43]

A quantitative description of the SOC- and height-dependant reactivity is shown in Figure S6 (Supporting Information). The SEI produced consists primarily of inorganic Na_2CO_3, and contains only ~5–10% organic species. Even though SIB SEIs are reported to have higher inorganic concentrations than those in LIBs,[12] this is still a lower ratio than expected based on experiments. Solvent dimerization and polymerization induced by reactions of $LiPF_6$ and H_2O have been reported experimentally in literature for similar Li-based systems.[44,45] It has also been reported that electrolytes with $NaPF_6$ generate SEIs with higher concentrations of organic species.[14] This indicates that $NaPF_6$ decomposition processes may involve the EC and PC species as well, which would explain the relatively low amount of organic species produced in the simulations. Overall, this discrepancy suggests that the presence of water contamination has a dramatic effect on SEI composition, which corresponds to degradation behavior reported in the literature[46] and may explain the relative inconsistency of SIB SEI compositions reported in the literature.

In this work, the "local" electrical potential corresponds to the potential of a given layer in the kMC cell relative to the Na/Na^+, further detail can be found in the methodology section. The red lines in Figure 1 correspond to the local electrical potential of the electrolyte (SEI and liquid), of a given *z*-layer at the time when the snapshots were taken. In the initial stages, the potential curve is disordered (Figure 1i), due to high reactivity and interface instability. The curve becomes more smooth after the initial SEI layers form and the system becomes less reactive. Also, the slope of the curve becomes less steep over time as the SEI becomes thicker. This behavior corresponds to the electric conductivity of the SEI, and will be discussed in more detail later. A significant discontinuity is observed at the SEI/electrolyte interface due to the resistance of conducting electrons across the SEI/electrolyte interface. This discontinuity corresponds to the electrical double layer.

2.2. Effects of Electrolyte Composition

Three different systems with varied electrolyte composition, 1:1, 9:1, and 1:9 EC:PC mass ratios, were studied in order to determine the influence of PC on the SEI. The three systems exhibited unexpectedly similar behavior, as shown in **Figure 2**. In each system the SEI grows at a similar rate to a maximum thickness of ≈26 nm at SOC = 100%, visible in Figure 2i, which is well within the range of values reported in the literature.[18,47]

The SEI in all three systems is composed of 90–97% (by mole) inorganic Na_2CO_3 (Figure 2ii), and the remaining organic phase

is composed of EG and dimers. The 1:1 and 1:9 EC:PC systems exhibit very similar behavior, indicating that, until a certain threshold, PC concentration does not have a substantial effect on the chemistry of the SEI. The 9:1 EC:PC system (C) has the highest ratio of inorganic to organic species in the SEI; this is primarily due to the lower favorability of the dimerization of EC intermediates. Carbonate formation dominates the reactions in all three systems, but the source of the carbonate species is significantly different for the different mixtures. The ratio of EC:PC consumed by carbonate formation is ≈0.6, 0.1, and 5 for EC:PC ratios of 1:1, 1:9, and 9:1, respectively (Figure 2iii), indicating a relatively similar reactivity for each species. This may contribute to the different organic:inorganic ratios observed experimentally, as the PC intermediates are more likely to polymerize compared to their corresponding EC intermediates.[48]

The inflection point in the potential (Figure 2iv) and in the degradation and intercalation reactions (Figure 2vi) occurs early (at ≈0.04 SOC) in all systems, and is triggered when the potential of the first layer on top of the carbon surface reaches ≈0.27 V (Figure S5, Supporting Information), which appears to mark the potential where Na^+ intercalation becomes energetically feasible and begins to compete with SEI-formation. The potential of the surface layer drops and reaches an equilibrium near 0.1 SOC, at which point intercalation becomes the dominant process of Na^+ consumption (Figure 2iv,v,vi). One would expect the "equilibrium" potential of the surface to move to 0 V as intercalation reactions began to dominate, rather than the ≈0.10–15 V (relative to Na/Na^+) observed in all three systems. This is because the potential corresponds to the first SEI layer, not the electrode itself. The difference from the expected potential here is likely related to the energy required for ion migration across the SEI/anode interface and into the electrode bulk. Future studies will focus on obtaining more detailed information and kinetic parameters for these processes.

The spatial potential, Figure 2vii, displays similar behavior over time for each system, i.e., it is not notably dependent on the EC:PC ratio. The increase and subsequent decrease at the SEI/electrolyte interface, most clearly visible in the SOC = 0.07 curves, corresponds well to the trends expected in the electrical double layer. The potential of the electrode / SEI interface stays relatively constant after it reaches a steady-state value, but the potential at the SEI/electrolyte interface continues to increase, which indicates that the system is not yet stable at the end of the first charge, and that SEI growth will continue; this corresponds well with the observed trends in reactivity (Figure 2vi).

The SEI in each system grew thicker not only due to continued reactivity, but also due to diffusive and dissolution effects. Figure 2viii shows the fraction of sites occupied by SEI species on a given layer near the beginning and at the end of charging. The high concentration of species initially near the surface diffuses and dissolves away over time, creating a thicker and more porous SEI layer. This reveals that the SEI actively dissolves and degrades even during initial formation. Dissolution and diffusion are discussed in more detail in a later section.

The similar behavior we observe between the systems with varied solvent composition indicates that PC concentration has a relatively small effect on SEI growth and composition. Instead, the worsened behavior reported experimentally is likely due to modification of the Na^+ solvation structure, resulting in changes to ionic transport behavior and (de)solvation at the electrode interface.[49,50]

2.3. Effects of Electrochemical Properties and Operating Conditions

Systems with modified SEI electronic conductivities (D,E), and C-rates (F,G), were modeled in order to study the influence of electrochemical conditions on SEI formation. The changes in electrochemical conditions induced much more significant effects on the systems than the changes in electrolyte composition, as shown in **Figure 3**.

Interestingly, the system charged at high C-rate (C = 1, G) exhibited the thinnest and most dense SEI, 15 nm at SOC = 1, and lowest electrolyte consumption (Figure 3i,iii,vii). This is likely because the high C-rate induced more dramatic fluctuations in potential at low SOC, followed by a constantly lower potential at higher SOCs (Figure 3iv; S3, Supporting Information), which increases the relative favorability of Na^+ intercalation. This behavior is in agreement with recent experimental work, which observed the formation of denser and thinner SEIs and higher cell capacities in SIBs when higher c-rates were applied during formation.[30] However, the dramatic change in potential at low SOCs also increased the relative favorability of glycol-forming reactions, leading to a SEI that is made of substantially more organic species than the other systems (Figure 3ii). These organic species are less stable and more soluble, and thus the generated SEI is likely to be less stable over time. Further evidence of the instability can be seen in Figure S7 (Supporting Information), where the reaction rate at SOC = 1 is substantially higher than with other systems. Additionally, the high C-rate means that the SEI species have had less time to diffuse and dissolve; when normalized to time instead of SOC, the SEI is the second thickest out of the systems tested (Figure S4i, Supporting Information). These are likely to be some of the underlying mechanisms behind the lower capacity retention during aging that has been observed experimentally with high C-rates.[28] This leads us to describe SEIs that are thinner and have greater inorganic compositions as higher quality.

The system charged at low C-rate (C/10, F) displayed the opposite behavior; it had the thickest SEI, 37 nm at SOC = 1, and high electrolyte consumption (Figure 3i,iii). It also had the least dramatic potential fluctuation and highest equilibrium potential, which favors carbonate-forming reactions, and generated an SEI with the highest inorganic concentration of the systems tested (Figures 3ii,iv; Figure S3, Supporting Information). The inorganic species are less likely to diffuse and dissolve; when normalized for time instead of SOC, the SEI for C/10 is the second thinnest out of the systems tested (Figure S4i, Supporting Information). This corresponds to a more robust SEI, and is likely responsible for the higher capacity retention associated with low C-rates.[28] However, the slow formation time also leads to an excessive consumption of active material during the first cycle (Figure 3v). This excess consumption corresponds to the lower initial capacity observed experimentally for low C-rates.[30]

The electric conductivities of the SEI were modified in order to study the benefits of a more or less "ideal" SEI.[51] The system with the electronic conductivity of the SEI doubled (E) exhibited

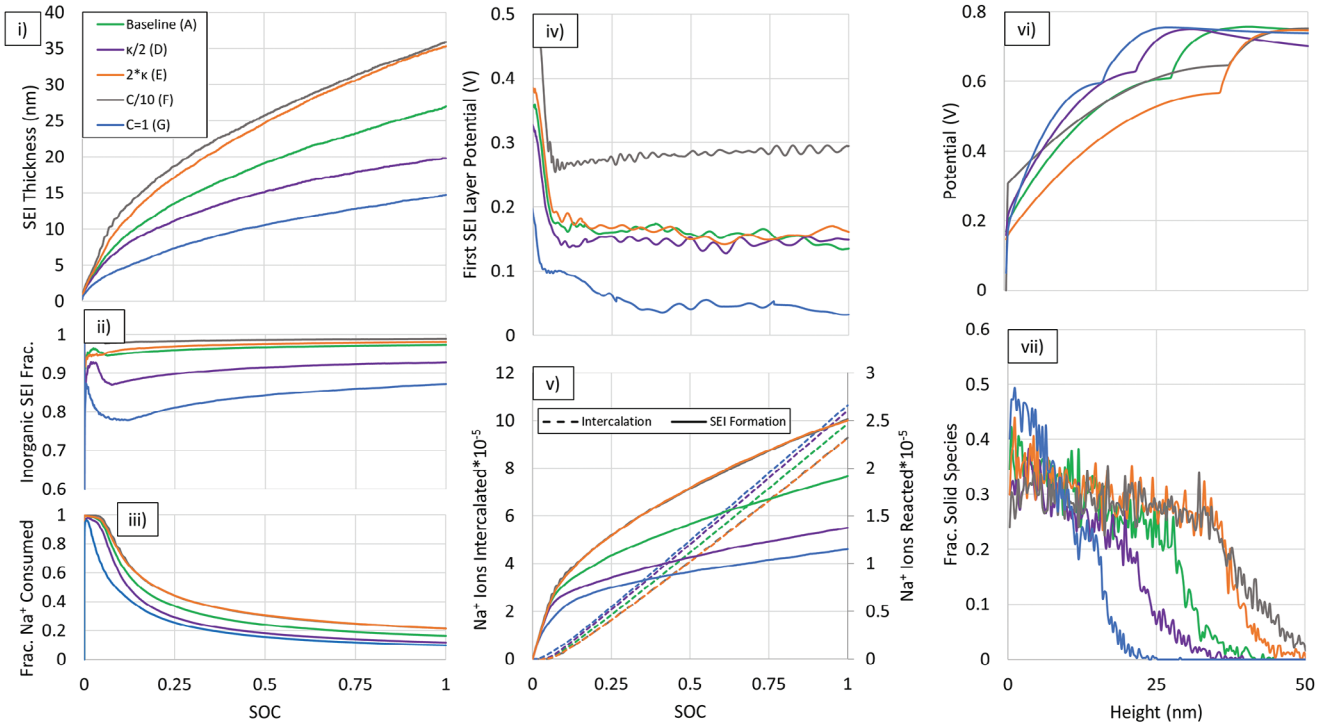

Figure 3. Impact of electrochemical properties and operating conditions on SEI evolution and properties (systems A/D/E/F/G) during a full charge. i) SEI thickness, ii) molar fraction of the SEI that is inorganic, iii) molar fraction of Na^+ consumed for SEI formation, iv) potential of the first SEI layer at the electrode surface, v) amount of Na^+ ions consumed by intercalation and SEI formation reactions, vi) spatial potential of each system at the end of the simulation, and vii) the fraction of sites occupied by solid species at a given height at SOC = 1.

the second thickest SEI at full charge (thickest relative to time, Figure 3i; Figure S4i, Supporting Information). Further, it has the second-highest ratio of Na^+ consumption via SEI formation versus intercalation. The high conductivity allowed for easier distribution of charge through the SEI, which, in turn, allowed for relatively higher potentials and increased the favorability of carbonate formation. This generates a SEI that is more stable against solubility, but is still reactive due to the high conductivity.

The system with the electronic conductivity of the SEI set to half of the baseline (D), presented the opposite behavior of (E), with the second thinnest SEI (thinnest relative to time), and a higher ratio of Na^+ consumption via intercalation. The SEI contained noticeably more organic species than other systems due to the low electronic conductivity causing more dramatic changes in potential (Figure S3, Supporting Information), increasing the likelihood of organic-forming reactions. This increased presence of organics indicates that low SEI conductivity can also have negative effects on the SEI. Further work could direct SEI design toward materials with conductivities low enough to reduce reactivity, but not so low that it induces the potential spikes that cause unfavorable reactions.

The local potential at the SEI/electrolyte interface at SOC = 1 has a similar value of ≈0.6 for all of the systems, regardless of SEI thickness or other conditions (Figure 3vi). There appears to be a slight proportional relationship between the potential at the SEI/electrolyte interface and electrical conductivity, which corresponds to the reduced reactivity observed with strongly insulating SEIs.

The kMC model reproduces the experimentally-observed phenomena; systems with low electronic conductivity produce high-quality SEIs, and that high C-rates can generate thin SEIs and reduce the consumption of active material during formation. The model results also suggest the production of excess organic species as a reason behind the worsened long-term capacity retention. This serves to validate the model's ability to reproduce electrochemical behavior and provide molecular-scale insight into the fundamental mechanisms behind battery-scale electrochemical behavior. This can be used to optimize first-formation protocols to find the ideal C-rates that maximize battery stability and minimize production costs and time. The SEI behaviors observed with these modified C-rates indicates that the first formation rate could be tuned to maximize the formation of stable SEI components, but minimize the unnecessary consumption of active material.

2.4. Effects of Diffusion and Dissolution

The possibility of dissolution as a primary mechanism of failure for SIB SEIs was explored by studying systems with varied diffusion rates (H,I,J) and with a uniform Na_2CO_3 initial SEI (K). Systems H and I correspond to SEIs that are highly soluble, and system J corresponds to a system where only the organic species are highly soluble. The "solubilities" in systems I and H are modified by changing the global diffusion rate prefactor in order to examine the influence of species that are more able to diffuse

Table 2. Variables and values used in kMC calculations.

Variable	Definition	Value
ΔL, d, r	Distance between sites, distance between lattice layers, average particle radius - estimated	4.1, 2.89, $2 \cdot 10^{-10}$ m
EB_{ii}, EB_{io}, EB_{is}, EB_{oo}, EB_{os}, EB_{ss}	Pairwise binding energies for inorganic (i), organic (o), and solvent (s) - estimated	2.64, 2.45, 1.9, 2.3, 1.8, 2.1 kcal mol^{-1} (3.9, 2.4, 1.8, 1.9, 1.3, 1.4 for system J)
$k_{0,\ Di/C/EC}$	Prefactors for diffusion, chemical, electrochemical reactions - chosen	$2 \cdot 10^{-9}$, 10^{13}, 10^{6}
D_{elec}	Diffusion coefficient for Na^+ in the electrolyte	$1.21 \cdot 10^{-10}$ m^2 s^{-1}[52]
D_{SEI}	Diffusion coefficient for Na^+ in the SEI	$1.69 \cdot 10^{-10}$ m^2 s^{-1}[53]
η	Solvent viscosity	0.00192 Pa·s[54]
R	Gas constant	8.314 J mol^{-1} K^{-1}
α	Charge transfer coefficient	0.5
F	Faraday's constant	96,845 C mol^{-1}
e	Elementary Charge	$1.602 \cdot 10^{-19}$ C
χ	Gravimetric capacity of hard carbon	386 mAh g^{-1}[55]
a_{sp}	Specific surface area of hard carbon	4 m^2 g^{-1}[56]
p_{el}	Electron tunneling constant	$-4.6 \cdot 10^{9}$ m^{-1}
A_s	Cross-sectional area of the cell	$5.45 \cdot 10^{-17}$ m^2
κ_S, κ_i, κ_e	Electronic conductivity of Na_2CO_3 - literature, interface, electrolyte-estimated	$1.05 \cdot 10^{-10}$,[57] $3 \cdot 10^{-11}$, $2 \cdot 10^{-12}$ S m^{-1}

away from their neighbors. The "solubility" of system J was modified by increasing the binding energies of inorganic species and decreasing the binding of organic species, which corresponds to inorganic species that are more strongly bound to each other and less likely to diffuse, and organic species that are less strongly bound to each other and more likely to diffuse. These modified values were chosen in order to provide an estimate at the influence of inorganic vs organic solubility, since the exact diffusion and binding properties of the species are not well-understood. Specific values are shown in **Table 2**. These conditions had a less dramatic effect on the system than the electrochemical properties, but still significantly influenced the SEI characteristics, as shown in **Figure 4**.

The system with doubled global diffusion rate ($k_{0,Di} = 4 \cdot 10^{-9}$, H), had the second thickest SEI in this set before SOC = 0.1, and the thickest SEI until SOC = 0.35, however, the rate of SEI growth subsequently decreased more than other systems, and system H exhibited the second-thinnest SEI at SOC = 1 (Figure 4i). The high diffusion rate caused the initial SEI species to rapidly diffuse away from the electrode and form a less dense, but thicker, SEI at low SOCs. This thick SEI became less conductive and blocked solvent species from nearing the lower potential layers at the electrode surface, and instead forced reactions to occur further away, at higher potentials, which increased the amount of inorganic species.

The system with the global diffusion rate increased to five times that of the baseline ($k_{0,Di} = 1 \cdot 10^{-8}$, I), exhibited similar behavior to system H, but to a higher degree. The SEI initially grew very quickly (Figure 4i), but then became the thinnest and most inorganic out of the systems I–K at SOC = 1. This is due in part to the same early insulating behavior as system H, but also due to a significant amount of species diffusing away from the electrode and dissolving. This resulted in a very porous SEI, with less than 1/4 of sites being occupied by solid species, and higher amounts of SEI components near the electrolyte phase, as visible in Figure 4vii. The long-term degradation effects from this porous SEI start to become evident as the system approaches SOC = 1. The system I initially had significantly fewer SEI-forming reactions than the other systems, but over time the porous SEI eventually became less insulating compared to the other systems, where more robust SEIs were formed. The effect of this is evident in Figure 4v as the systems approach full charge. Here, the rate of SEI forming reactions in the system I does not decrease as significantly as it does for other systems, as indicated by the increased slope relative to the other systems. This corresponds well to the uncontrolled SEI growth expected for highly soluble and unstable SEIs.

System J, where organic diffusion was increased and inorganic diffusion was left constant, formed a SEI of similar thickness to that of system H, but exhibited significantly more reactivity (Figure 4v). This means system J has the most dense SEI out of the systems in this group, i.e., the high amount of SEI species formed in system J were distributed in a relatively thin SEI, however, it also indicates that the decreased reactivity observed in the system H was also caused, in part, by the increased inorganic diffusion creating a thicker SEI.

Interestingly, the system with the 2 nm thick native Na_2CO_3 SEI, K, has the highest concentration of organic species (Figure 4ii). This occurred because the native SEI initially insulated against all reactions, which caused the local potential to spike and increase the relative favorability of glycol-forming reactions. After the system stabilizes, it has the lowest reactivity and highest intercalation ratio at low SOC (Figure 4iii) of systems I–K. In spite of this, K had the thickest SEI out of the studied systems as the simulation approached SOC = 1. This is due to the highly soluble organic species diffusing away from the electrode and dissolving. Overall, the behavior of system K reinforces the effectiveness of uniform artificial SEIs,[58,59] but also indicates that

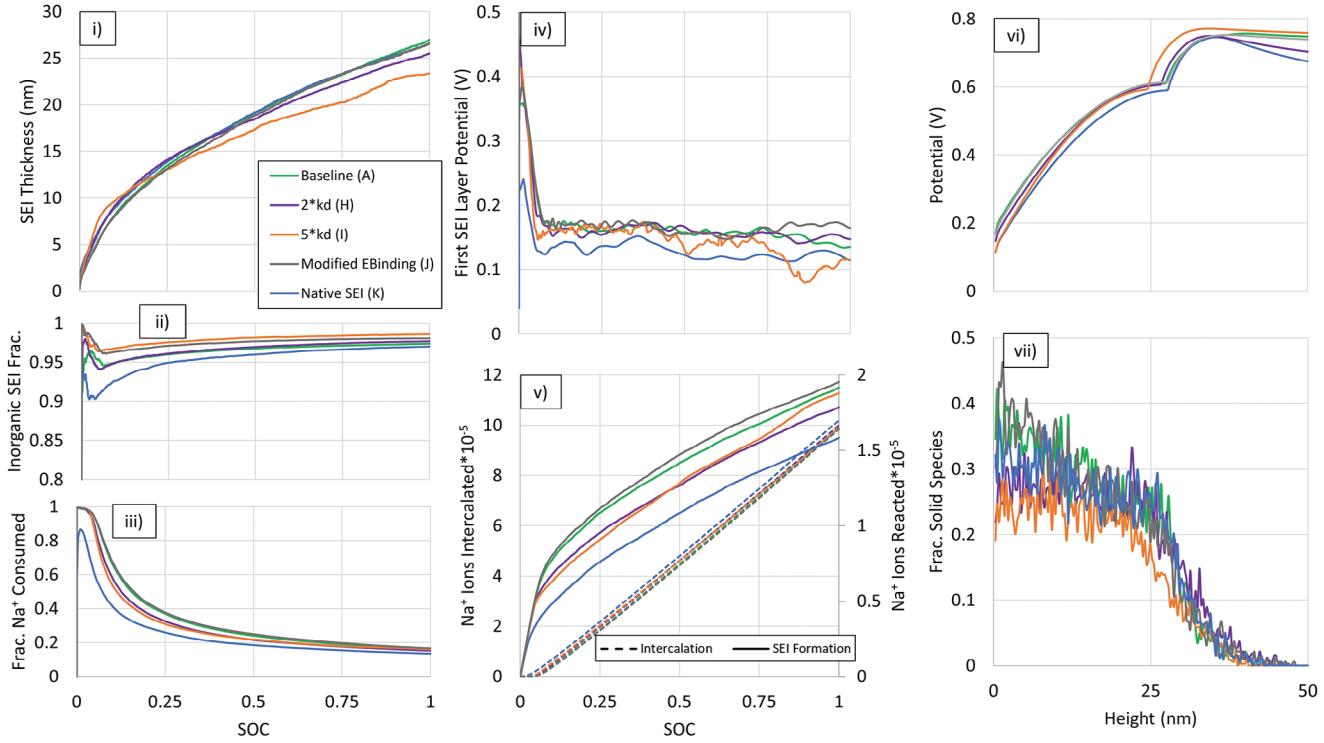

Figure 4. Impact of diffusion and native SEI (systems A/H/I/J/K) on SEI growth and properties during a full charge. i) SEI thickness, ii) mole fraction of the SEI that is inorganic, iii) molar fraction of Na^+ consumed for SEI formation, iv) the potential of first SEI layer at the electrode surface, v) amount of Na^+ ions consumed by intercalation and SEI formation reactions, vi) spatial potential of each system at SOC = 1, and vii) fraction of solids at a given height at SOC = 1.

special care should be taken at the beginning of the first charge in order to compensate for the lowered reactivity of the interface and ensure stability of the system.

The behavior of these systems corresponds well to what is expected; highly soluble species create initially thicker and more porous SEIs. These thick SEIs may initially inhibit reactivity, but eventually become relatively less insulating and can facilitate uncontrolled SEI degradation over time.

3. Conclusion

The kMC model developed in this work is able to provide novel and detailed molecular-scale insights on SEI growth, properties, and dissolution on a hard carbon anode during the first charge formation step. This model was developed in a generalized structure so that it can easily be extended to new systems and chemistries, such as Na-metal electrodes and impurities, in order to study their unique SEI growth and behavior.

The model has revealed that $NaPF_6$ decomposition and NaF formation are not favorable at standard conditions, and impurities such as water are required to initiate the reaction. It is also likely that these $NaPF_6$ decompositions, would they occur, facilitate dimerization and polymerization of electrolyte species. The ratio of solvents in EC:PC electrolytes has little effect on the chemical composition of the SEI, and the experimentally observed benefits of higher EC content are likely related to more complex changes in solubility or ionic transport.

The model was able to accurately replicate the complex influences of electrochemical properties and cell operating conditions on SEI behavior. SEIs with low electric conductivities exhibit the most ideal behavior. High C-rates generate thinner SEIs and have lower irreversible first charge capacity loss due to consumption of the active material, but also increase the formation of less-stable organic species, which is likely responsible for reduced long-term capacity retention.

We were able to observe the initial failure of the SEI due to dissolution. Highly-soluble species generate thick and porous SEIs that begin to degrade even as they are forming, leading to uncontrolled electrolyte consumption and capacity loss.

This model lays the groundwork for understanding the nanoscale mechanisms that guide SEI growth, and facilitates the understanding of detailed relationships between system conditions, SEI properties, and cell behavior, that can be used to tune the formation of stable and effective SEIs and guide the development of next-generation SIBs.

4. Experimental Section

Chemistry and Reaction Network: A reaction network for the species present in the electrolyte, EC/PC/$NaPF_6$, was initially estimated based on known reaction pathways in similar Li-ion systems.[42,60] This network consisted of carbonate, glycol, and dimer formation reactions of EC/PC, as well as NaF formation. DFT calculations were then employed to determine the specific decomposition pathways and mechanisms. It is known that also impurities such as H_2O are inside experimental electrolytes and may trigger additional reactions, as in Li-based batteries.[61] Yet, taking

additives and impurities into account will blur the picture on understanding the main interaction of electrolyte and surface. The study here thus provides a solid fundamental understanding and a base for extension with additives and impurities. The overall reaction pathways used in the kMC simulations are shown below:

$$EC + 2Na^+ + 2e^- \longleftrightarrow Na_2CO_3 + C_2H_4 \quad (1)$$

$$EC + 2Na^+ + 2e^- \longleftrightarrow NaO(CH_2)_2ONa + CO \quad (2)$$

$$PC + 2Na^+ + 2e^- \longleftrightarrow Na_2CO_3 + C_3H_6 \quad (3)$$

$$2EC + 2Na^+ + 2e^- \longleftrightarrow NaCO_3(CH_2)_2CO_3Na + C_2H_4 \quad (4)$$

$$2PC + 2Na^+ + 2e^- \longleftrightarrow NaCO_3CH_2CH(CH_3)CO_3Na + C_3H_6 \quad (5)$$

$$EC + PC + 2Na^+ + 2e^- \longleftrightarrow NaCO_3(CH_2)_2CO_3Na + C_3H_6 \quad (6)$$

$$EC + PC + 2Na^+ + 2e^- \longleftrightarrow NaCO_3CH_2CH(CH_3)CO_3Na + C_2H_4 \quad (7)$$

$$PC + 2Na^+ + 2e^- \longleftrightarrow Na_2CO_3 + C_3H_6 \quad (8)$$

$$PC + 2Na^+ + 2e^- \longleftrightarrow Na_2CO_3 + C_3H_6 \quad (9)$$

$$PF_6^- + 3Na^+ + 3e^- \longleftrightarrow PF_3 + 3NaF \quad (10)$$

These pathways were split into a total of 25 separate reaction steps, and their corresponding reverse reactions, that were able to occur in the simulations. The full list of reaction steps and kinetic parameters can be found in Table S1 (Supporting Information).

Kinetic Monte Carlo Model: In this work, a prior kMC model was adapted to include dynamic and spatially-dependent local potentials in order to accurately simulate interface conditions during charging. The potentials were not set, but rather controlled by the system current and electrochemical reactions, allowing for precise study of electrochemical phenomena. All kMC systems in this study were 18 x 18 x 220 sites (~10 x 10 x 64 nm), on Face Centered Cubic (FCC)-style lattices with periodic boundaries on the x- and y-axis, and bulk boundary conditions on the z-axis. A (FCC)-style lattice was employed in order to improve computational efficiency; each site has 12 equidistant neighbors, which reduces the number of rate equations compared to body-centered/simple cubic configurations, allowing for faster calculation times. The distance between lattice sites was set at 0.41 nm, based on the size of a solvent molecule. The distance between lattice layers was 0.289 nm, based on the distance between FCC sites. Solid species were able to diffuse through the upper *z*-boundary and permanently leave the cell.

All systems were studied at 1 atm and 298 K, with a 1 M $NaPF_6$ concentration. KMC simulations were performed using Matlab version R2022a.[62] The Ovito software package was used to visualize geometric kMC results.[63]

The kMC model used in this work was adapted from previous models developed by the group.[36,38,41,64] The model was powered by the variable step size method, where the time steps of each calculation step were varied based on the available event rates, allowing for the study of long timescales.[65,66] The structured list algorithm, which calculates all possible reaction rates in the system, was employed in order to substantially increase calculation speed.[67] This algorithm is described in more detail in the Supporting Information. The possible events in the kMC code and their governing rate equations, are as follows:

Diffusion Γ_D, which is based on the pairwise binding energies between the diffusing species and its neighbors.[64,68]

$$\Gamma_D = \frac{k_{0,Di}}{\Delta L^2} \cdot D \cdot \exp\left(\frac{-(\Sigma n_{zi}E_{b,zi} + \Sigma n_{zj}E_{b,zo} + \Sigma n_{zs}E_{b,zs})}{RT}\right) \quad (11)$$

Here, $n_{zi/zo/zs}$ are the number of inorganic, organic, and solvent neighbors of the diffusing species z ($z = i$ / o / s), $E_{b,zi/zo/zs}$ are the binding energies between species z and inorganic i, organic o, and electrolyte s species. The binding energies considered are limited to general inorganic, organic, and solvent interactions, as the computational cost of accounting for all possible pairwise interactions is not currently feasible. The binding energy for inorganic–inorganic was based on results from DFT calculations of Na_2CO_3 vacancy diffusion, all other binding energies were estimated based relative to this value. R is the gas constant, $k_{0,Di}$ is the frequency factor for diffusion, ΔL is the distance between lattice sites, and T is the system temperature. D is diffusion coefficient based on the Stokes–Einstein–Sutherland equation:

$$D = \frac{k_b T}{6\pi r \eta} \quad (12)$$

Here, k_b is Boltzmann's constant, r is the average particle radius, and η is the electrolyte viscosity. A value of $k_{0,Di}$ was selected that produced realistic behavior while minimizing computational cost. This value was also varied during the study in order to examine diffusivity. It should be noted that this selection of $k_{0,Di}$, along with the assumed binding energies, makes it challenging to be certain about diffusion behavior. Future work would aim to work with experimental groups to develop more precise diffusion parameters.

In addition to the diffusion mode explained above, Na^+ species were also able to move vertically toward the electrode via electromigration in the electrolyte $\Gamma_{Em,\,elec}$ and the SEI $\Gamma_{Em,\,SEI}$. Na^+ might also transport through and occupy the same sites as SEI species:

$$\Gamma_{Em,elec} = \frac{k_{0,Di}}{\Delta L^2} \cdot D_{elec} \cdot \left(\frac{e\nu\Delta\phi_{elec}}{k_b T} + \Delta c_{elec}\right) \quad (13)$$

$$\Gamma_{Em,SEI} = \frac{k_{0,Di}}{\Delta L^2} \cdot D_{SEI} \cdot \left(\frac{e\nu\Delta\phi_{elec}}{k_b T} + \Delta c_{SEI}\right) \quad (14)$$

Here, F is Faraday's constant, d is the distance between lattice layers, ν is the valency of the species, and $D_{elec/SEI}$ are the diffusion coefficients for cation diffusion across the electrolyte and SEI. Δc_{elec} and $\Delta\phi_{elec}$ are the concentration and potential differences across the electrolyte, respectively, and are intended to account for the Coulombic interactions of the solvent as well as the potential influence. These were calculated based on the difference between the average concentration and potential in the bulk of the electrolyte and the average concentration and potential in the bulk of the SEI. Δc_{SEI} and $\Delta\phi_{SEI}$ are the concentration and potential differences across the SEI, respectively. These were calculated based on the difference between the average concentration and potential in the bulk of the SEI and the concentration and potential at the SEI/electrode interface, divided by d. The additional concentration term is included in order to help disperse Na^+ and improve local electroneutrality, since the $NaPF_6^-$ anion is evenly distributed throughout the system.

Forward and backward chemical reaction rates $\Gamma_{fwd/bwd}$ were calculated using the standard Arrhenius-type equations:

$$\Gamma_{fwd} = k_{0,C} \cdot \exp\left(\frac{-E_A}{RT}\right) \quad (15)$$

$$\Gamma_{bwd} = k_{0,C} \cdot \exp\left(\frac{-E_A + \Delta G}{RT}\right) \quad (16)$$

Here, $k_{0,C}$ is the frequency factor for chemical reactions, E_a is the activation energy and ΔG is the reaction free energy.

Electrochemical reaction rates $\Gamma_{red/ox}$ were calculated based on Butler–Volmer kinetics:

$$\Gamma_{red} = k_{0,EC} \cdot \exp\left(\frac{-E_A}{RT}\right) \exp\left(\frac{-(1-\alpha)F(\phi_{l,n} - \phi_{0,z})}{RT}\right) \quad (17)$$

$$\Gamma_{ox} = k_{0,EC} \cdot \exp\left(\frac{-E_A + \Delta G}{RT}\right) \exp\left(\frac{\alpha F(\phi_{l,n} - \phi_{0,z})}{RT}\right) \quad (18)$$

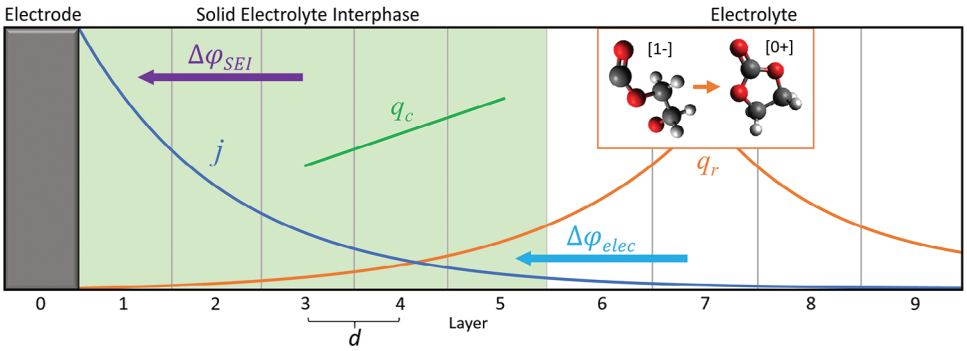

Figure 5. Schematic of electrical flux distribution in kMC cell. The curves correspond to how the influence of current, reactivity, and conductivity is distributed throughout the cell. The grey layer corresponds to the electrode, green layers correspond to the SEI. Grey, red, and white atoms correspond to carbon, oxygen, and hydrogen, respectively.

Here, α is the charge transfer coefficient, $\phi_{l,\,n}$ is the "local" potential of the layer n where the reaction is taking place, and $\phi_{0,\,z}$ is the reduction potential of the reactant species z. All values of ϕ_0 were calculated with DFT and set in reference to Na/Na^+. $k_{0,EC}$ is the frequency factor electrochemical reactions, which was set to 10^6 instead of the standard 10^{13} in order to avoid excessive forward and backward red/ox reactions at equilibrium, this substantially decreased calculation time, but did not affect the overall behavior of the systems, e.g., instead of having 50 forward and 49 backward reactions in a given time, there may be 8 forward and 7 backward, leading to the same overall net reactivity.[69]

Additionally, cation intercalation into the electrode Γ_{int} was treated as a separate irreversible electrochemical reaction. This reaction was able to occur when a cation was within the SEI and had at least one SEI neighbor, and the "local" potential of the reaction was taken to be the potential at the SEI/electrode interface ($\phi_{l,\,1}$ or $\phi_{l,\,2}$). Intercalation was assumed to be essentially instantaneous via the "knock-off" mechanism,[70] where a Na^+ near the top of the SEI displaces a Na^+ bound to a SEI component, which subsequently displaces another Na^+, until a Na^+ in the bottom-most SEI layer migrates to the electrode.

$$\Gamma_{int} = k_{0,EC} \cdot \exp\left(\frac{-(1-\alpha)F(\phi_{l,1/2} - \phi_{0,Na^+})}{RT}\right) \tag{19}$$

Electroneutrality is controlled by regularly varying the local potential ϕ_l of each layer n in the system according to the following charge balance equation:

$$\frac{d\phi_{l,n}}{dt} = C_p(Ip_{el,n} - Fq_{r,n} + q_{c,n}) \tag{20}$$

where C_p is a proportional controller constant used to ensure numerical stability. The applied current I is calculated based on the C-rate, gravimetric capacity χ, and specific surface area of hard carbon, a_{sp}, of the system using the equation:

$$I = \frac{C_{rate} \cdot \chi}{a_{sp}} \tag{21}$$

This flux is distributed to each layer of the cell using an exponential decay function, $p_{el,\,n}$, that corresponds to a 1% probability of electron tunneling to a location 1nm from the electrode surface.

$$p_{el,n} = \exp(p_{ed}(n - n_{ref})d) \tag{22}$$

where p_{ed} is a constant for the function and n_{ref} is the reference layer that is acting on the given layer n. The same constant $p_{el,\,n}$ is used to distribute the electronic flux produced or consumed by reactions, $q_{r,n}$, on a given layer to its neighboring layers.

$$q_{r,n} = \sum_{k=1}^{n_{max}} p_{el,n-k}\frac{r_{red,k} - r_{ox,k}}{tA_sN_A} \tag{23}$$

where $r_{red/ox,k}$ are the numbers of reduction and oxidation reactions that occurred on layer k, N_A is Avogadro's number, t is time, and A_s is the cross sectional area of the cell.

The electronic flux on a given layer due to conductivity, $q_{c,n}$, is dependent on the potential differences between the given layer n and its neighboring layers, and the electric conductivity of the layer $\kappa_{S/i/e}$.

$$q_{c,n} = \frac{\kappa_{S/i/e}}{d} \cdot \Delta\phi_{n,n-1} + \frac{\kappa_{S/i/e}}{d} \cdot \Delta\phi_{n+1,n} \tag{24}$$

where κ_S corresponds to SEI layers, κ_i corresponds to SEI/electrolyte interface layers, and is intended to approximate resistance to electron conduction across the interface, and κ_e corresponds to the electrolyte and was chosen arbitrarily to ensure numerical stability. κ_e would be significantly higher in a real system, but including this caused substantial numerical problems, and had no noticeable influence on the system behavior, since reactions primarily occur in the SEI and interface. Future work would aim to improve the electrolyte conductivity in order to better represent the electrical double layer. In order to avoid numerical discontinuities at the intermediate layers between the SEI/interface/electrolyte, the conductivities κ_{Si} and κ_{ie} were calculated by treating the intermediate layer as a combination of the two conductors in series, proportional to their current compositions $\epsilon_{S/i/e}$ in the layer.

$$\kappa_{Si} = \frac{1}{\frac{1}{\epsilon_S\kappa_S} + \frac{1}{\epsilon_i\kappa_i}} \tag{25}$$

$$\kappa_{ie} = \frac{1}{\frac{1}{\epsilon_i\kappa_i} + \frac{1}{\epsilon_e\kappa_e}} \tag{26}$$

A schematic of the electronic flux distribution is shown below in **Figure 5**. For example, the local potential on layer 4 is influenced by tunneling from the system current proportional to $p_{t,\,4}$, tunneling from the reaction occurring at layer 7 proportional to $p_{t,\,3}$, and electronic conduction from layers 3 and 5. $\Delta\phi_{SEI}$ is the difference between the average of $\phi_{l,\,1/2}$ and the average of $\phi_{l,\,3/4/5}$ of divided by d. $\Delta\phi_{elec}$ is the difference between the average of $\phi_{l,\,3/4/5}$ and the average of $\phi_{l,\,6/7/8/9}$ divided by d.

The bulk diffusion of the electrolyte was assumed to be significantly faster than the processes in the kMC calculation, which allowed for the implementation of constant concentrations of electrolyte species. The electrolyte species were represented implicitly in the system by setting all unoccupied sites to have a constant probability of being EC, PC, and PF_6^-,

corresponding to their respective concentrations. This allows the explicit diffusion events of the electrolyte to be neglected and substantially reduces computational time. In order to represent the lowered likelihood of solvent species diffusing through a thick SEI, and to avoid implicit solvent appearing in voids generated deep in the SEI, the electrolyte concentration probability of unoccupied sites more than 4 nm deep in the SEI surface decreased exponentially, with a 99% reduction at 8 nm. For the purposes of thickness calculations, an SEI "layer" is defined as any layer in the kMC cell that is at least 1/3 occupied by solid SEI species, furthermore, layers that are less than 1/3 occupied are considered to contribute a proportional amount to the thickness, i.e. a layer that is 30% occupied will count as 0.9 SEI layers, and a layer that is 3% occupied will count as 0.1 SEI layers. This value was tuned based on the behavior of test simulations.

Density Functional Theory Calculations: All molecular DFT calculations were performed using the M06-2X exchange-correlation functional[71] with a 6-31+g(d,p) basis set.[72–79] The conductor-like polarizable continuum model (CPCM) implicit solvent method[80] with a dielectric constant of 81.17, corresponding to 1:1 EC:PC,[81] was used to represent the electrolyte. Energies for other implicit solvent compositions were not calculated because the energy barriers and reaction energies for the degradation of EC in EC and PC in PC are relatively similar to the mixture of EC/PC 1:1. This occurs because solvation models such as CPCM with high dielectric constant only consider the electronic contribution. For molecules in solvents with high dielectric values, the electronic properties of the molecules are relatively similar, even for high solvatochromie molecules.[82,83]

Reaction energies for $NaPF_6$ decomposition as well as reaction and activation energies for dimer formation were obtained using the Gaussian16 software package.[84] Activation energies were not calculated for $NaPF_6$, since they are known to be strongly dependent on solvent coordination, and obtaining values that are not unrealistically high is challenging. Instead, the $NaPF_6$ decomposition was assumed to be kinetically barrier-free, and only limited by electrochemical reduction, similar to what is observed for corresponding $LiPF_6$ systems.[42] Furthermore, the reaction energies and activation barriers for EC/Na and PC/Na degradation were calculated using ORCA Version 5.0.3.[85,86] A combination of the Nudged Elastic Band and Saddle Point Optimization (NEB-TS) was implemented to estimate the transition state (TS)[87] of the reactions and obtain the activation energies.

The energy barrier for Na_2CO_3 diffusion was calculated using the Vienna Ab-initio Simulation Package (VASP),[88,89] based on the projector-augmented wave pseudopotential formalism.[90] The Generalized Gradient Approximation (GGA) and Perdew–Burke–Ernzerhof (PBE) functional were used to compute the exchange-correlation terms.[91] Calculations were performed at the Gamma k-point, the convergence of the self-consistent field was set to a value of 10^{-6}, and a cutoff energy of 500 eV was used to expand the electron wave functions of the plane-wave basis set,[92] and a Gaussian smearing of 0.01 eV was used to accelerate convergence. A 17.9 × 16 × 11.98 Å(4 × 4 × 3) supercell was created with periodic boundaries extended in all three spatial directions. The geometry was initially optimized, then a Na_2CO_3 formula unit was removed in order to create a vacancy, and the geometry was optimized again. The energy barrier for diffusion was calculated using the Climbing-Image NEB method with the Quick-Min force optimizer.[93,94]

Supporting Information

Supporting Information is available from the Wiley Online Library or from the author.

Acknowledgements

This work was funded by the German Research Foundation (DFG) under Project ID 390874152 (POLiS Cluster of Excellence). M.H.P. and A.G. thank the DFG for financial support through Project C5 of the Transregional Collaborative Research Centre TRR234 CataLight (Project No.364549901). The authors acknowledge support by the state of Baden–Württemberg through bwHPC and the German Research Foundation (DFG) through grant no INST 40/575-1 FUGG (JUSTUS 2 cluster).

Open access funding enabled and organized by Projekt DEAL.

Conflict of Interest

The authors declare no conflict of interest.

Data Availability Statement

The data that support the findings of this study are openly available in KITopen at 10.35097/1957, reference number 1000169131.

Keywords

composition, dissolution, electrochemical kinetics, kinetic monte carlo, sodium-ion, solid electrolyte interphase

Received: March 13, 2024
Revised: July 30, 2024
Published online:

[1] P. A. Owusu, S. Asumadu-Sarkodie, *Cogent Eng.* **2016**, *3*, 1167990.
[2] L. Lu, X. Han, J. Li, J. Hua, M. Ouyang, *J. Power Sources* **2013**, *226*, 272.
[3] V. Etacheri, R. Marom, R. Elazari, G. Salitra, D. Aurbach, *Energy Environ. Sci.* **2011**, *4*, 3243.
[4] H. Pan, Y.-S. Hu, L. Chen, *Energy Environ. Sci.* **2013**, *6*, 2338.
[5] H. S. Hirsh, Y. Li, D. H. S. Tan, M. Zhang, E. Zhao, Y. S. Meng, *Adv. Energy Mater.* **2020**, *10*, 2001274.
[6] C. Yang, S. Xin, L. Mai, Y. You, *Adv. Energy Mater.* **2021**, *11*, 2000974.
[7] V. Palomares, P. Serras, I. Villaluenga, K. B. Hueso, J. Carretero-González, T. Rojo, *Energy Environ. Sci.* **2012**, *5*, 5884.
[8] Y. Sun, *Reuters* **2021**.
[9] C. Gauckler, M. Dillenz, F. Maroni, L. F. Pfeiffer, J. Biskupek, M. Sotoudeh, Q. Fu, U. Kaiser, S. Dsoke, H. Euchner, P. Axmann, M. Wohlfahrt-Mehrens, A. Groß, M. Marinaro, *ACS Appl. Energy Mater.* **2022**, *5*, 13735.
[10] M. Muñoz-Márquez, D. Saurel, J. L. Gómez-Cámer, M. Casas-Cabanas, E. Castillo-Martínez, T. Rojo, *Adv. Energy Mater.* **2017**, *7*, 1700463.
[11] R. Mogensen, D. Brandell, R. Younesi, *ACS Energy Lett.* **2016**, *1*, 1173.
[12] S. Komaba, W. Murata, T. Ishikawa, N. Yabuuchi, T. Ozeki, T. Nakayama, A. Ogata, K. Gotoh, K. Fujiwara, *Adv. Funct. Mater.* **2011**, *21*, 3859.
[13] D. Stottmeister, L. Wildersinn, J. Maibach, A. Hofmann, F. Jeschull, A. Groß, *ChemSusChem* **2024**, *17*, 202300995.
[14] G. G. Eshetu, T. Diemant, M. Hekmatfar, S. Grugeon, R. J. Behm, S. Laruelle, M. Armand, S. Passerini, *Nano Energy* **2019**, *55*, 327.
[15] M. Ma, H. Cai, C. Xu, R. Huang, S. Wang, H. Pan, Y.-S. Hu, *Adv. Funct. Mater.* **2021**, *31*, 2100278.
[16] X. Xia, J. R. Dahn, *J. Electrochem. Soc.* **2012**, *159*, A515.
[17] J. Fondard, E. Irisarri, C. Courrèges, M. R. Palacin, A. Ponrouch, R. Dedryvère, *J. Electrochem. Soc.* **2020**, *167*, 070526.
[18] M. Carboni, J. Manzi, A. R. Armstrong, J. Billaud, S. Brutti, R. Younesi, *ChemElectroChem* **2019**, *6*, 1745.
[19] Z. Wang, H. Yang, Y. Liu, Y. Bai, G. Chen, Y. Li, X. Wang, H. Xu, C. Wu, J. Lu, *Small* **2020**, *16*, 2003268.
[20] L. A. Ma, A. J. Naylor, L. Nyholm, R. Younesi, *Angew. Chem.* **2021**, *133*, 4905.

[21] Y. Jin, P. M. L. Le, P. Gao, Y. Xu, B. Xiao, M. H. Engelhard, X. Cao, T. D. Vo, J. Hu, L. Zhong, B. E. Matthews, R. Yi, C. Wang, X. Li, J. Liu, J.-G. Zhang, *Nat. Energy* **2022**, *7*, 718.
[22] Q. Liu, R. Xu, D. Mu, G. Tan, H. Gao, N. Li, R. Chen, F. Wu, *Carbon Energy* **2022**, *4*, 458.
[23] A. Ponrouch, E. Marchante, M. Courty, J.-M. Tarascon, M. R. Palacín, *Energy Environ. Sci.* **2012**, *5*, 8572.
[24] A. V. Cresce, S. M. Russell, O. Borodin, J. A. Allen, M. A. Schroeder, M. Dai, J. Peng, M. P. Gobet, S. G. Greenbaum, R. E. Rogers, K. Xu, *Phys. Chem. Chem. Phys.* **2017**, *19*, 574.
[25] D. Monti, E. Jónsson, A. Boschin, M. Rosa Palacín, A. Ponrouch, P. Johansson, *Phys. Chem. Chem. Phys.* **2020**, *22*, 22768.
[26] Z. Tian, Y. Zou, G. Liu, Y. Wang, J. Yin, J. Ming, H. N. Alshareef, *Adv. Sci.* **2022**, *9*, 2201207.
[27] C. Mao, S. J. An, H. M. Meyer, J. Li, M. Wood, R. E. Ruther, D. L. Wood, *J. Power Sources* **2018**, *402*, 107.
[28] S. J. An, J. Li, Z. Du, C. Daniel, D. L. Wood, *J. Power Sources* **2017**, *342*, 846.
[29] P. M. Attia, S. J. Harris, W. C. Chueh, *J. Electrochem. Soc.* **2021**, *168*, 050543.
[30] J. Sun, I. E. Gunathilaka, L. A. O'Dell, P. C. Howlett, M. Forsyth, *J. Power Sources* **2023**, *554*, 232298.
[31] D. Schäfer, K. Hankins, M. Allion, U. Krewer, F. Karcher, L. Derr, R. Schuster, J. Maibach, S. Mück, D. Kramer, R. Mönig, F. Jeschull, S. Daboss, T. Philipp, G. Neusser, J. Romer, K. Palanisamy, C. Kranz, F. Buchner, R. J. Behm, A. Ahmadian, C. Kübel, I. Mohammad, A. Samoson, R. Witter, B. Smarsly, M. Rohnke, *Adv. Energy Mater.* **2024**, *14*, 2302830.
[32] L. Alzate-Vargas, S. M. Blau, E. W. C. Spotte-Smith, S. Allu, K. A. Persson, J.-L. Fattebert, *J. Phys. Chem. C* **2021**, *125*, 18588.
[33] D. Witt, F. Röder, U. Krewer, *Batter. Superc.* **2022**, *5*, 202200067.
[34] F. Single, A. Latz, B. Horstmann, *ChemSusChem* **2018**, *11*, 1950.
[35] M. Andersen, C. Panosetti, K. Reuter, *Front. Chem.* **2019**, *7*, 202.
[36] J. Wagner-Henke, D. Kuai, M. Gerasimov, F. Röder, P. B. Balbuena, U. Krewer, *Nat. Commun.* **2023**, *14*, 6823.
[37] K. Hankins, E. P. Kamphaus, P. B. Balbuena, **2021**, *397*, 139272.
[38] F. Röder, R. D. Braatz, U. Krewer, *Comput. Chem. Eng.* **2019**, *121*, 722.
[39] F. Röder, V. Laue, U. Krewer, *Batter. Superc.* **2019**, *2*, 248.
[40] H. Euchner, A. Groß, *Phys. Rev. Mater.* **2022**, *6*, 040302.
[41] M. Gerasimov, F. A. Soto, J. Wagner, F. Baakes, N. Guo, F. Ospina-Acevedo, F. Röder, P. B. Balbuena, U. Krewer, *J. Phys. Chem. C* **2023**, *127*, 4872.
[42] D. Kuai, P. B. Balbuena, *J. Phys. Chem. C* **2023**, *127*, 1744.
[43] P. Barnes, K. Smith, R. Parrish, C. Jones, P. Skinner, E. Storch, Q. White, C. Deng, D. Karsann, M. L. Lau, J. J. Dumais, E. J. Dufek, H. Xiong, *J. Power Sources* **2020**, *447*, 227363.
[44] B. L. D. Rinkel, D. S. Hall, I. Temprano, C. P. Grey, *J. Am. Chem. Soc.* **2020**, *142*, 15058.
[45] J. Henschel, C. Peschel, S. Klein, F. Horsthemke, M. Winter, S. Nowak, *Angew. Chem. Int. Ed.* **2020**, *59*, 6128.
[46] F. Baakes, M. Lüthe, M. Gerasimov, V. Laue, F. Röder, P. B. Balbuena, U. Krewer, *J. Power Sources* **2022**, *522*, 230881.
[47] A. M. Tripathi, W.-N. Su, B. Joe Hwang, *Chem. Soc. Rev.* **2018**, *47*, 736.
[48] I. A. Shkrob, Y. Zhu, T. W. Marin, D. Abraham, *J. Phys. Chem. C* **2013**, *117*, 19270.
[49] J. Li, S. Huang, P. Yu, Z. Lv, K. Wu, J. Li, J. Ding, Q. Zhu, X. Xiao, J. Nan, X. Zuo, *J. Colloid Interface Sci.* **2024**, *657*, 653.
[50] T. Cai, Y. Wang, F. Zhao, Z. Ma, P. Kumar, H. Xie, C. Sun, J. Wang, Q. Li, Y. Guo, J. Ming, *Adv. Energy Mater.* **2024**, *14*, 2400569.
[51] M. Broussely, S. Herreyre, P. Biensan, P. Kasztejna, K. Nechev, R. J. Staniewicz, *J. Power Sources* **2001**, *97-98*, 13.
[52] D. Morales, L. G. Chagas, D. Paterno, S. Greenbaum, S. Passerini, S. Suarez, *Electrochimica Acta* **2021**, *377*, 138062.
[53] L.-Y. Kuo, A. Moradabadi, H.-F. Huang, B.-J. Hwang, P. Kaghazchi, *J. Power Sources* **2017**, *341*, 107.
[54] K. Hayamizu, *J. Chem. Eng. Data* **2012**, *57*, 2012.
[55] R. R. Gaddam, E. Jiang, N. Amiralian, P. K. Annamalai, D. J. Martin, N. A. Kumar, X. S. Zhao, *Sustainable Energy Fuels* **2017**, *1*, 1090.
[56] KURANODE|kuraray, https://www.kuraray.com/products/lithium (accessed: January 2024).
[57] H. Näfe, *ECS J. Solid State Sci. Technol.* **2013**, *3*, N7.
[58] H. Wang, Y. Tang, *Chem. Res. Chin. Univ.* **2020**, *36*, 402.
[59] Q. Liu, A. M. Rao, X. Han, B. Lu, *Adv. Sci.* **2021**, *8*, 2003639.
[60] Y. Wang, P. B. Balbuena, *J. Phys. Chem. B* **2002**, *106*, 4486.
[61] X. He, D. Bresser, S. Passerini, F. Baakes, U. Krewer, J. Lopez, C. T. Mallia, Y. Shao-Horn, I. Cekic-Laskovic, S. Wiemers-Meyer, F. A. Soto, V. Ponce, J. M. Seminario, P. B. Balbuena, H. Jia, W. Xu, Y. Xu, C. Wang, B. Horstmann, R. Amine, C.-C. Su, J. Shi, K. Amine, M. Winter, A. Latz, R. Kostecki, *Nat. Rev. Mater.* **2021**, *6*, 1036.
[62] T. M. Inc, MATLAB version: 9.12.0.1956245 (R2022a), **2022**, https://www.mathworks.com (accessed: February 2024).
[63] A. Stukowski, *Modell. Simul. Mater. Sci. Eng.* **2009**, *18*, 015012.
[64] F. Röder, R. D. Braatz, U. Krewer, *J. Electrochem. Soc.* **2017**, *164*, E3335.
[65] A. P. J. Jansen, *An Introduction to Kinetic Monte Carlo Simulations of Surface Reactions*, Vol. *856*, Springer, New York **2012**.
[66] J. Grotendorst, N. Attig, I. for Advanced Simulation, editors, *Multi-scale simulation methods in molecular sciences: winter school, 2-6 March 2009, Forschungszentrum Jülich, Germany; lecture notes*, Number 42 in NIC series / John von Neumann Institute for Computing, Supercomputing Centre, Forschungszentrum Jülich, Jülich, **2009**.
[67] T. P. Schulze, *Phys. Rev. E* **2002**, *65*, 036704.
[68] J. D. Tucker, R. Najafabadi, T. R. Allen, D. Morgan, *J. Nucl. Mater.* **2010**, *405*, 216.
[69] M. Stamatakis, D. G. Vlachos, *Comput. Chem. Eng.* **2011**, *35*, 2602.
[70] S. Shi, P. Lu, Z. Liu, Y. Qi, L. G. J. Hector, H. Li, S. J. Harris, *J. Am. Chem. Soc.* **2012**, *134*, 15476.
[71] Y. Zhao, D. G. Truhlar, *Theor. Chem. Acc.* **2007**, *120*, 215.
[72] J.-P. Blaudeau, M. P. McGrath, L. A. Curtiss, L. Radom, *J. Chem. Phys.* **1997**, *107*, 5016.
[73] V. A. Rassolov, M. A. Ratner, J. A. Pople, P. C. Redfern, L. A. Curtiss, *J. Comput. Chem.* **2001**, *22*, 976.
[74] V. A. Rassolov, J. A. Pople, M. A. Ratner, T. L. Windus, *J. Chem. Phys.* **1998**, *109*, 1223.
[75] R. C. Binning, L. A. Curtiss, *J. Comput. Chem.* **1990**, *11*, 1206.
[76] M. M. Francl, W. J. Pietro, W. J. Hehre, J. S. Binkley, M. S. Gordon, D. J. DeFrees, J. A. Pople, *J. Chem. Phys.* **1982**, *77*, 3654.
[77] R. Ditchfield, W. J. Hehre, J. A. Pople, *J. Chem. Phys.* **1971**, *54*, 724.
[78] P. Hariharan, J. Pople, *Mol. Phys.* **1974**, *27*, 209.
[79] W. J. Hehre, R. Ditchfield, J. A. Pople, *J. Chem. Phys.* **1972**, *56*, 2257.
[80] V. Barone, M. Cossi, *J. Phys. Chem. A* **1998**, *102*, 1995.
[81] M. S. Ding, *J. Electrochem. Soc.* **2003**, *150*, A455.
[82] M. H. Putra, B. Bagemihl, S. Rau, A. Groß, *Chem. - Eur. J.* **2024**, *30*, 202302643.
[83] M. H. Putra, S. Seidenath, S. Kupfer, S. Gräfe, A. Groß, *Chem. - Eur. J.* **2021**, *27*, 17104.
[84] M. J. Frisch, G. W. Trucks, H. B. Schlegel, H. B. Schlegel, G. E. Scuseria, M. A. Robb, J. R. Cheeseman, G. Scalmani, V. Barone, G. A. Petersson, H. Nakatsuji, X. Li, M. Caricato, A. V. Marenich, J. Bloino, B. G. Janesko, R. Gomperts, B. Mennucci, H. P. Hratchian, J. V. Ortiz, A. F. Izmaylov, J. L. Sonnenberg, D. Williams-Young, F. Ding, F. Lipparini, F. Egidi, J. Goings, B. Peng, A. Petrone, T. Henderson, et al., Gaussian, **2016**.
[85] F. Neese, *WIREs Comput. Mol. Sci.* **2022**, *12*, 5.
[86] F. Neese, *WIREs Comput. Mol. Sci.* **2011**, *2*, 73.
[87] V. Ásgeirsson, B. O. Birgisson, R. Bjornsson, U. Becker, F. Neese, C. Riplinger, H. Jónsson, *J. Chem. Theory Comput.* **2021**, *17*, 4929.

[88] G. Kresse, J. Hafner, *Phys. Rev. B* **1993**, *47*, 558.
[89] G. Kresse, J. Furthmüller, *Comput. Mater. Sci.* **1996**, *6*, 15.
[90] G. Kresse, D. Joubert, *Phys. Rev. B* **1999**, *59*, 1758.
[91] J. P. Perdew, K. Burke, M. Ernzerhof, *Phys. Rev. Lett.* **1996**, *77*, 3865.
[92] G. Kresse, J. Furthmüller, *Phys. Rev. B* **1996**, *54*, 11169.
[93] G. Henkelman, B. P. Uberuaga, H. Jónsson, *J. Chem. Phys.* **2000**, *113*, 9901.
[94] D. Sheppard, R. Terrell, G. Henkelman, *J. Chem. Phys.* **2008**, *128*, 134106.